Available online at www.sciencedirect.com
ScienceDirect
C. R. Mecanique 337 (2009) 528–538
COMPTES RENDUS MECANIQUE

Combustion for aerospace propulsion

Large-Eddy Simulation of transcritical flows

T. Schmitt [a,*], L. Selle [b], B. Cuenot [a], T. Poinsot [b]

[a] *CERFACS, 42, avenue Gaspard-Coriolis, 31057 Toulouse cedex 01, France*
[b] *Institut de mécanique des fluides de Toulouse, allée du Professeur-Camille-Soula, 31400 Toulouse, France*

Available online 23 July 2009

Abstract

The present study uses the LES code AVBP, developed at CERFACS, to simulate transcritical flows. Real gas effects are accounted for by the use of a cubic equation of state, in conjunction with appropriate viscosity and thermal conductivity coefficients. First a single nitrogen round jet at supercritical pressure injected in a gaseous reservoir is simulated. Two cases are considered, one demonstrating a transcritical injection (high density injection), the other being directly injected at supercritical temperature (lower density injection). Comparison with available measurements shows good agreement. Finally, the simulation of a reacting case from the Mascotte bench (ONERA) is performed, consisting in a single coaxial injector injecting transcritical oxygen and supercritical hydrogen in a 60 bar chamber. Mean flow characteristics are in good agreement with the experimental observations of OH* emission, whereas temperature comparisons are more difficult to interpret. ***To cite this article: T. Schmitt et al., C. R. Mecanique 337 (2009).***
© 2009 Published by Elsevier Masson SAS on behalf of Académie des sciences.

Résumé

Simulation aux Grandes Echelles d'écoulements transcritiques. L'étude est basée sur l'utilisation du code de Simulation des Grandes Echelles AVBP, développé au CERFACS, pour simuler des écoulements transcritiques. Les effets gaz réels sont modélisés via une équation d'état cubique et des coefficients de viscosité et de conductivité thermique appropriés. D'abord, un jet rond axisymétrique à pression supercritique injecté dans un réservoir gazeux est simulé. Deux cas d'injection sont considérés : l'un en condition transcritique (densité élevée à l'injection) et l'autre à température supercritique (densité faible à l'injection). Un bon accord avec les expériences disponibles est constaté. Finalement, la simulation d'un cas Mascotte réactif (ONERA), où l'oxygène et l'hydrogène sont respectivement injectés en condition transcritique et supercritique dans une chambre à 60 bars, est présenté. Le calcul est en bon accord avec les résultats expérimentaux d'émission de OH*. La comparaison des températures le long de la couche de mélange est plus délicate à interpréter. ***Pour citer cet article : T. Schmitt et al., C. R. Mecanique 337 (2009).***
© 2009 Published by Elsevier Masson SAS on behalf of Académie des sciences.

Keywords: Combustion; Computational fluid mechanics; Large-Eddy Simulation; Supercritical

Mots-clés : Combustion ; Mécanique des fluides numérique ; Simulation des grandes échelles ; Supercritique

* Corresponding author.
E-mail address: thomas.schmitt@cerfacs.fr (T. Schmitt).

1631-0721/$ – see front matter © 2009 Published by Elsevier Masson SAS on behalf of Académie des sciences.
doi:10.1016/j.crme.2009.06.022

1. Introduction

Fluids encountered in cryogenic rocket engines and advanced gas turbines or internal combustion engines may be at supercritical pressure condition, i.e. at a pressure higher than the critical pressure of the mixture. In such conditions, fluid behavior may strongly differ from that of a perfect gas [1,2].

Over the past ten years, the need to get a better understanding of high pressure systems resulted in numerous studies on supercritical fluids. Both AFRL (Air Force Research Laboratory) and DLR (Deutsches Zentrum für Luft- und Raumfahrt) experimentally studied round jets at supercritical pressure [3–5]. The impact of the supercritical pressure on the jet topology was demonstrated, showing that rather than breaking into several drops, the ligaments classically observed in two phase jet dissolve in the ambient gas, with no longer evidence of drops creation. A further increase in pressure leads to a more perfect-gas-like jet. The influence of acoustic perturbations was also studied [6], highlighting their reduced effect in supercritical conditions in comparison with subcritical environment, suggesting that the coupling mechanism between acoustics and jets may be different for supercritical pressure jets than for subcritical pressure jets.

Cryogenic rocket engines at supercritical pressure were experimentally tested using LOx/GH2 [7–9], LOx/CH4 and LOx/LCH4 [10]. Using OH^* emission, Candel et al. [7] investigated the role of the momentum flux ratio between LOx and GH2 on the shape of the flame, showing that increasing the ratio reduces the spreading angle of the flame, i.e. an opposite behavior than in subcritical conditions. Singla et al. [11] obtained instantaneous and average distribution of OH radicals thanks to the use of OH planar laser-induced fluorescence, showing the wrinkling of the flame due to turbulence interaction along the mixing layer.

Because of the tremendous difficulties associated with high pressure measurements, data are, at the present time, restricted to OH^* emission fields [7,11], shadowgraph [8,7] and Coherent Anti-Stokes Raman Scattering (CARS) temperature [8,12]. Unfortunately, no quantitative information about the velocity field is available.

This topic was also studied numerically, in particular with direct numerical simulation of mixing layers, showing the role of density gradients on the global layer stability and turbulence characteristics and the strong effect on the molecular mixing of the reduced species diffusion near critical conditions [13]. This highlighted the need for appropriate subgrid-scale models for Large Eddy Simulation (LES) under supercritical pressure conditions [14]. Reynolds-Averaged Navier–Stokes (RANS) simulations of the Mascotte test rig [15] have been performed by Demoulin et al. [16].

Only few LES have been performed under transcritical conditions. An extensive review of the non-reacting LES up to 2006 can be found in Zong and Yang [17]. A single nitrogen round jet was studied by Zong [18,19]. The stabilizing effect of the density gradient, and its role on turbulent energy redistribution along the mixing layer was identified. Shear coaxial injection and mixing of oxygen and methane has also been simulated by Zong and Yang [20].

A shear coaxial LOx/GH2 jet flame at supercritical pressure was investigated by both Matsuyama [21] and Oefelein [22], highlighting that the flame stabilization mechanism near the injector lips is linked to the presence of a strong recirculation zone of burnt gases.

Unfortunately, all these reacting simulations were in the vicinity of the injector lips. The objective of the present study is to build a real gas LES solver that can compute large configurations with intricate geometries. This is achieved by using the AVBP solver, in conjunction with appropriate thermodynamics, equation of state and transport coefficients.

Section 2 is devoted to the presentation of the AVBP LES solver and the necessary modifications for real gas implementation. Then Section 3 presents the validation of the solver on single nitrogen round jet cases [4] under supercritical pressure. Finally, Section 4 describes the simulation of case C60 of the Mascotte test rig [8].

2. Methodology and models for LES of transcritical combustion

2.1. Description of the LES solver

The unstructured explicit solver AVBP is used to compute the compressible Navier–Stokes equations for a multi-species gas [23]. A third order (in time and space) low dissipative centered scheme [24] is used to obtain accurate turbulence intensities [25]. Because of the high density gradients encountered in transcritical systems, artificial viscosity is used to avoid spurious oscillations [26]. Note that, compared to the original formulation of Jameson [26], the

sensor is modified to work on density and be less dissipative. The 2nd order artificial dissipation operator is built to manage gradient by keeping the local pressure untouched. Characteristic boundary conditions are set with the NSCBC method [27,23], adapted to the real gas thermodynamics. For reacting case, the dynamically thickened flame model (TFLES) is used [28], in conjunction with a 2 steps–4 species kinetic scheme for H_2/O_2, adapted from the work of Rogers and Chinitz [29].

2.2. Real-gas thermodynamics

In this study, the Peng–Robinson [30] equation of state is used to model the high pressure thermodynamics:

$$P = \frac{\rho r T}{1 - \rho b_m} - \frac{\rho^2 a_m}{1 + 2\rho b_m - \rho^2 b_m^2} \tag{1}$$

where T is the temperature, P the pressure, ρ the density, $r = R/W$ with R being the gas constant and W the molar mass, $a_m(T)$ and b_m are the Peng–Robinson coefficients, that depend on the critical values of the substances involved in the computation and the mixture. The latter coefficients are computed using the classical Van Der Waals mixing rule. Details may be found in Poling et al. [2]. Comparisons with the NIST database for pure species show very good agreement in the critical zone and for temperature higher than the critical temperature. Nevertheless, 10% errors on the density appear in the dense zone.

Changing the equation of state has consequences on the thermodynamic behavior, and all thermodynamic coefficients, that are linked to the equation of state [2], are computed using the Peng–Robinson equation of state. Complete formulations for the computation of internal energy, sound speed, ... may be found in [1]. Note that, for consistency reasons, modified thermodynamics have an impact on the formulation of boundary conditions and Jacobian matrices of the numerical schemes.

2.3. Assumptions and subgrid-scale (SGS) models

Pressure gradient contribution on the heat flux and temperature gradient effect on mass flux may become significant in high pressure situations. The so-called Dufour and Soret effects have nevertheless been neglected in the present study, since: (1) in the scope of LES simulation SGS fluxes are predominant prior to laminar fluxes; and (2) Oefelein [31], using (fine) LES results indicate only weak effects of these additional terms. The heat flux is then computed using the classical Fick's law for heat conduction and inter-diffusion because heat transport through species diffusion. Species diffusion fluxes are computed using the Hirschfelder–Curtiss approximation [1].

Transport coefficients also show considerable changes when real gas effects are important. Here, the method proposed by Chung et al. [32] is used to compute the viscosity and thermal conductivity. Choosing the same method for both viscosity and thermal conductivity allows a significant gain on computational time. The model is based on a low pressure, perfect gas formulation, corrected with an empirical expression to account for high density effects. Used in conjunction with the Peng–Robinson equation of state [30], the model gives good results when compared to the NIST database. Detail of the formulation can be found in [32] or [2]. Calculating mass diffusion coefficients is a difficult task in supercritical regime, and no reliable methodology exists. A detailed discussion is given in [33]. At the moment, constant, species dependent, Schmidt numbers are used.

SGS modeling in supercritical systems is still an open question. Selle et al. [14] and Bellan [13] point out that the generally neglected sub-grid terms in low pressure cases may become important at high pressure. They also highlight the necessity to take into account the strong non-ideality of the thermodynamics and transport terms in the models. However, no closure for sub-grid terms is available today and classical closure models are used here, such as the WALE model [34], which take into account local strain and rotation rates and provides low dissipation in pure shear zones. This model allows a better jet destabilization and more resolved turbulence and therefore better statistics.

The SGS energy and mass fluxes are modeled using the gradient transport assumption with turbulent Schmidt and Prandtl numbers set to 0.6.

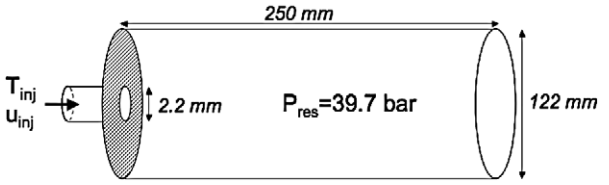

Fig. 1. Sketch of the experiment of Mayer et al. [4].

Table 1
Injection conditions [4].

Case	T_{inj} [K]	u_{inj} [m s^{-1}]	T/T^*	$\frac{\rho_{inj}}{\rho_\infty}$	Re_{inj}
3	126.9	4.9	0.98	9.6	1.7×10^5
4	137	5.4	1.06	3.7	1.6×10^5

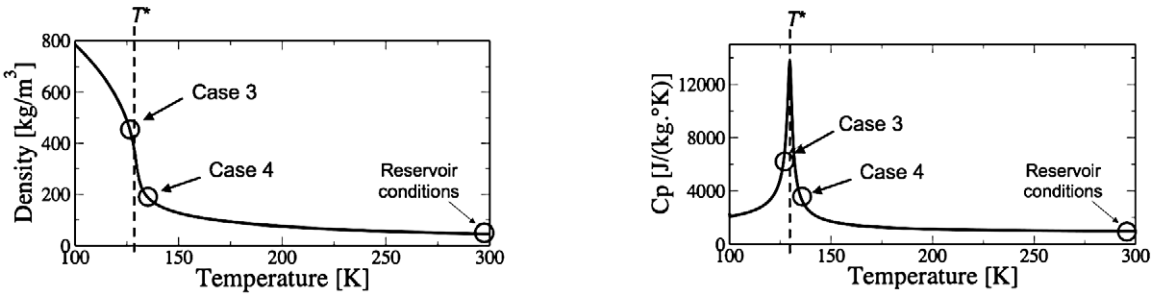

Fig. 2. Density and heat capacity for the two test cases.

3. LES of transcritical round jet

As a first step towards the simulation of reacting systems, a simulation of a round nitrogen jet at supercritical pressure is performed. The configuration corresponds to the experimental setup of DLR for the study of cryogenic systems [4].

3.1. Flow configuration

The configuration is made of a single round jet injected in a cylindrical reservoir (Fig. 1) pressurized at 40 bar with a temperature initially at 298 K. Two cases are computed, corresponding to cases 3 and 4 in Mayer et al. [4], summarized in Table 1.

The main difference between the two cases is the injection temperature T_{inj}, which is to be compared to the pseudo-boiling temperature T^*. The pseudo-boiling temperature is the temperature at which, for a given pressure, the heat capacity at constant pressure reaches its maximum. In this case, the reservoir pressure is 39.7 bar and the corresponding pseudo-boiling temperature is 129.5 K (see Fig. 2). In case 3, the injection temperature, $T_{inj,3} = 126.9$ K, is slightly below the pseudo-boiling temperature T^*, while, for case 4, the temperature $T_{inj,4} = 137$ K is slightly higher than the pseudo-boiling temperature. Near the pseudo-boiling point, properties of the fluid are known to be strongly sensitive to the temperature [35,1], so that, for case 3, the injection density $\rho_{inj,3} = 435$ kg m^{-3}, is much higher than for case 4, $\rho_{inj,4} = 171$ kg m^{-3}, whereas in the reservoir, density is equal in both cases to $\rho_\infty = 45.5$ kg m^{-3}. This leads to strong density ratios between the jet and the ambient fluid ($\rho_{inj}/\rho_\infty = 9.6$ for case 3 and $\rho_{inj}/\rho_\infty = 3.7$ for case 4).

It should also be pointed out that, because of the strong increase in the dynamic viscosity near the pseudo-boiling temperature, the Reynolds numbers at injection for case 3 and case 4 are similar (Table 1).

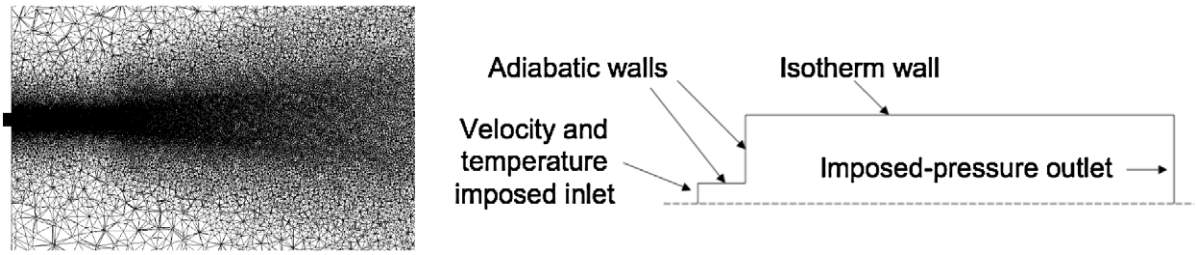

Fig. 3. Plane cut of the mesh over a length of 30 injector diameters (left) and sketch of the boundary conditions used in the simulation (right).

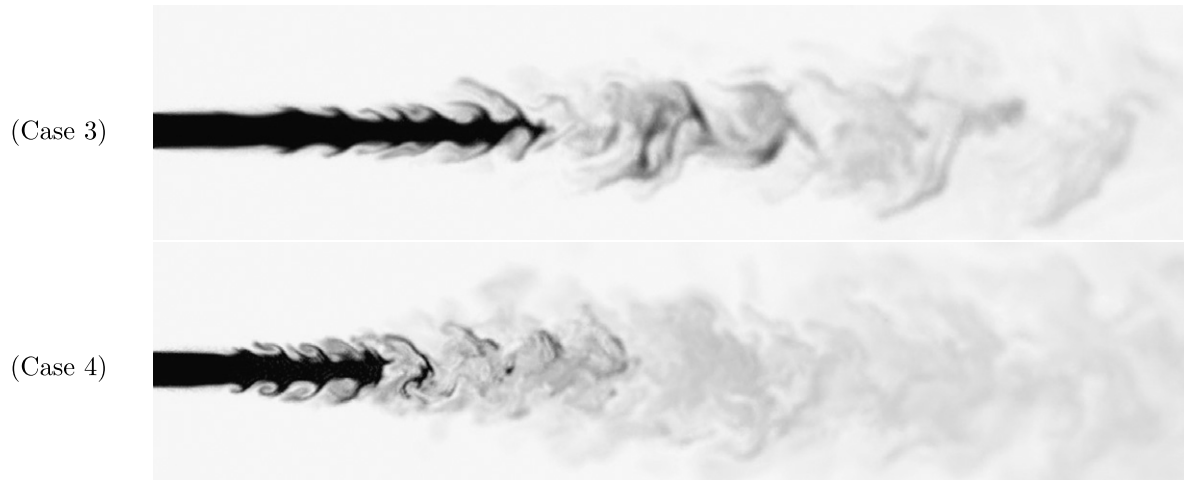

Fig. 4. Instantaneous cuts of density in the near injector zone (30 diameters). White: 45 kg/m^3; Black: 435 kg/m^3 (case 3) and 171 kg/m^3 (case 4).

3.2. Numerical setup

The computational domain consists in a cylindrical reservoir, with a diameter of 122 mm. The diameter of the round injector is 2.2 mm. A planar cut of the mesh is shown in Fig. 3 (left). The grid is refined near the injector, with a constant cell size of 0.1 mm on a distance of almost 10 diameters. This zone is followed by a smooth coarsening region towards the exit. The mesh contains 950 000 points and 5 500 000 tetrahedra.

Boundary conditions are also depicted in Fig. 3 (right). The pressure in the reservoir is maintained by a non-reflecting outlet with imposed pressure. The walls near the injector are modeled as adiabatic. The outer walls of the reservoir are isotherm, with an imposed temperature of 298 K. Velocity and temperature are imposed at the inlet. Turbulent perturbations are added to the mean flow at the inlet using the procedure of Kraichnan/Smirnov [36,37], with an intensity of 2.5%, which is a typical value for turbulent round jets.

3.3. Results and discussion

3.3.1. Flow visualization

Fig. 4 shows two cuts, for cases 3 and 4, of an instantaneous density field. As presented in Section 3.1, the injection density for case 3 (435 kg m^{-3}) is much higher than for case 4 (171 kg m^{-3}). The two jets are both affected by large Kelvin–Helmholtz like vortical structures. However, case 3, which has a much larger density is less affected than case 4 and the eventual destruction of the inner dense core is slower.

In case 3, stretched structures emerge from the central core. The structures, generally referred to as ligaments, are typical of transcritical jets, and have been previously evidenced in experiments [3].

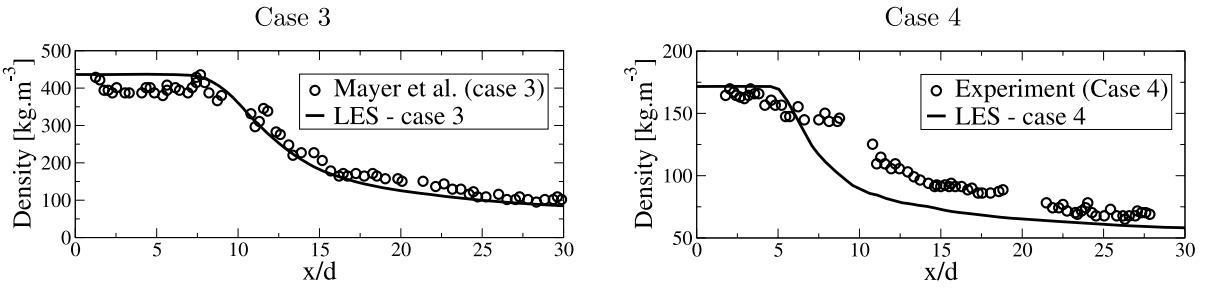

Fig. 5. Comparison between experimental and LES results of the center-line density in terms of normalized distance from the injector. Left: case 3; Right: case 4.

Table 2
Tangent of the spreading angle obtained by LES, and comparisons with experimental results of Mayer et al. [4] and Oschwald and Micci [38]. Angles are computed between $x/d = 15$ and $x/d = 25$.

Case	LES	Experiment [4]	Oschwald and Micci [38]
3	0.227	0.196	0.206
4	0.241	–	0.312

The mixing layer seems to be stabilized by the density gradient, since structures need a longer distance to develop in case 3 than in case 4. Note the strong injection temperature dependence of supercritical flows in the vicinity of the critical temperature, since it only differs of 10 K between case 3 and case 4, but behaviors are highly different.

3.3.2. Comparison with experimental data

Because of the very high pressure, only few data concerning the density field are available. Measurements have been performed using 2-D Raman imaging, giving informations on density and spreading angle [4].

Comparisons of the center-line density of the computation with the experimental results obtained by Mayer et al. [4] at DLR, for case 3 and case 4, are shown in Fig. 5. Results compare fairly well with the experiment for case 3. Differences between measured and computed density in the potential core zone (i.e. where the density keeps its injection value) for case 3 is due to the tendency of Raman imaging technique to predict lower density values when density is very high (see Mayer et al. [4]). However, case 4 shows important discrepancies with the experimental results. They may originate from the strong uncertainty on the injection temperature (see Mayer et al. [4]), which has a strong influence on the injection density and then on the potential core length (Fig. 2, left). Note that the dense-core length is around 7.9 diameters for case 3 and falls to 5.1 diameters for case 4 (taken at 99% of the injection density).

The tangent of the spreading angle of density is given in Table 2, obtained by linear interpolation of the Full Width Half Maximum (FWHM) of density between $x/d = 15$ and $x/d = 25$ (Oschwald and Micci [38]). The FWHM is the width of the jet measured between the 2 median density values. Computation is in good agreement with the experimental observations for case 3. FWHM of density was not available for the case 4. LES results are also compared with other results from similar experiments of Oschwald et al. [38,35] in Table 2. LES results for case 3 are in good agreement with experiments, while, for case 4, simulation indicates a lower spreading angle than the measurements of Oschwald and Micci [38]. Contrary to experiments, LES shows weak influence of the density ratio at injection on the spreading rate of the jet for $x > 15d$. The strong variability of the measurements outlined in Oschwald et al. [35] (see Figs. 17 and 18) between each experiment highlight the strong uncertainties in high-pressure systems.

4. LES of reacting coaxial LOx/GH2 injector

This section is devoted to the simulation of a reacting coaxial LOx/GH2 injector, using the experimental results of the Mascotte test rig (case C60) [15]. The Mascotte cryogenic combustion test facility is operated by ONERA to study fundamental processes involved in the combustion of cryogenic propellants.

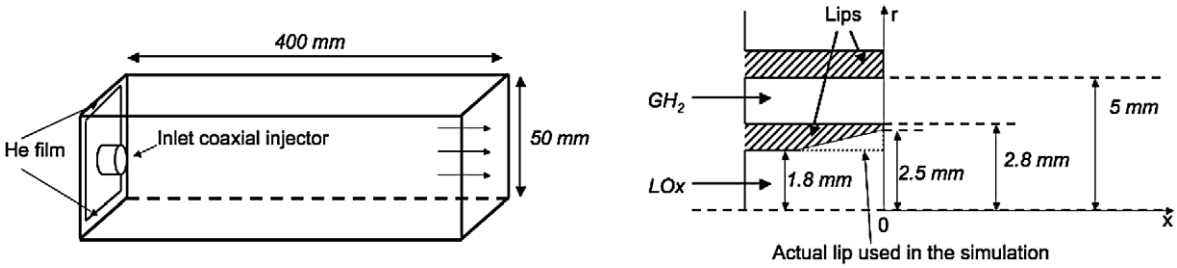

Fig. 6. Sketch of the computational domain (left). Sketch of the coaxial injector (right). Mascotte case.

Table 3
Injection conditions for the Mascotte case.

Species	Mass flux [g/s]	T_{inj} [K]	T_c [K]	P_c [bar]	ρ_{inj} [kg/m^3]
O_2	105	83	154	50.4	1340
H_2	42	275	33	12.8	5.25
He	24.5	280	5.19	2.27	10

4.1. Flow configuration

The domain (Fig. 6, left) is a 50 mm × 50 mm square-section box. The total length is 400 mm. The outlet nozzle used in the experiment is replaced by a non-reflecting constant-pressure outlet in the simulation. A helium film is injected along the side walls for cooling purpose. The coaxial injector, and its dimensions, are represented in Fig. 6 (right). Note that the initially tapered lip is replaced by a rectangular one. The width of the lip used in the computation is 1 mm.

Boundary conditions are given in Table 3 and the pressure in the domain is 6 MPa. Note that the oxygen is injected in transcritical state, while hydrogen is gaseous. The global equivalence ratio is very rich ($\phi = 3.2$). The corresponding mass flux ratio E is 2.5. Because the lips between oxygen and hydrogen are wider, the momentum flux ratio J is 1.43 whereas it is 4 in the experiment. This parameter is known to influence the initial spreading of the flame in coaxial systems [7]. Nevertheless, the effect seems to be more limited in supercritical systems when compared with subcritical cases [7,39] so that it is expected not to notably alter the result considering the purpose of the current study.

4.2. Numerical setup

The simulation is performed on a tri-dimensional domain containing 850 000 nodes and 5 000 000 tetrahedra, based on prior experience. Walls are adiabatic. Turbulent perturbations on velocity, corresponding to a turbulence intensity of 3% of the mean flow, are imposed in oxygen and hydrogen injectors.

4.3. Results and discussion

4.3.1. Instantaneous fields

An instantaneous iso-surface of temperature taken at 2000 K, colored by the axial velocity, is plotted in Fig. 7. The length of the view is 200 mm. One can notice the strong shear between the outer – light and fast – hydrogen and the central oxygen jet. Downstream the injector, after 50–60 mm, a strong change in the dynamics occurs. Indeed, the initially low-spreading jet, widens quickly together with the rapid transformation of small intense vortical structures into larger vortices.

The hydrogen mass-fraction field is presented in Fig. 8, with iso-lines of heat release. The hydrogen jet is initially deviated by the thermal expansion of the central dense jet and destabilizes few millimeters after injection, exhibiting intense vortical structures. On the contrary, the dense oxygen jet is stable until 60 mm.

The heat-release iso-contours of Fig. 8 show that the flame topology is close to the oxygen jet behavior, with an initially low spreading angle, until 60 mm, with no appearance of vortices, followed by the apparition of large structures. After 90 mm, the flame is still open. The heat release is higher by at least 1 order of magnitude (from

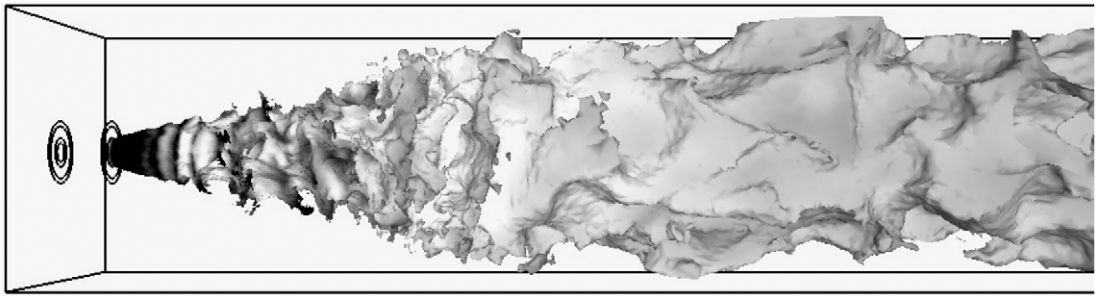

Fig. 7. Iso-contour of temperature (2000 K) colored by (saturated) axial velocity (black: 100 m/s; white: 0 m/s; length of view = half of the total length). Actual axial velocity reaches 150 m/s in the hydrogen outer flow.

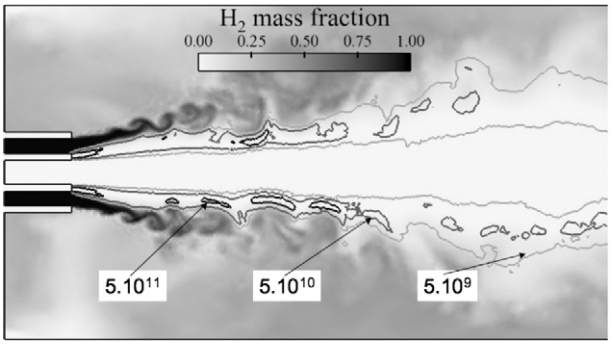

Fig. 8. Section of the hydrogen mass fraction field in the median plan of the domain (length of view ≈ 90 mm) and iso-contours of heat release (5×10^9, 5×10^{10} and 5×10^{11} W/m^3).

5×10^9 to 5×10^{10} W/m^3) in the first 60 mm than at 90 mm, mainly due to the strong shear between the fast hydrogen jet (≈140 m/s) and the central jet (≈7.8 m/s). Moreover, as indicated by the presence of heat release pockets equal to 5×10^{11}, the vortical structures locally enhance the heat release, highlighting the importance of dynamics in the combustion processes occurring in the mixing layer.

The heat release iso-contours also indicate that the flame is anchored to the lips. This is consistent with experimental observations [39]. The stabilization is associated with an intense reactive zone. The latter is able to attach to the lips because of the use of adiabatic boundaries and sufficient grid resolution. The study of the stabilization mechanisms is not the goal of this calculation.

4.3.2. Average fields and experimental comparisons

The mean OH mass fraction is shown in Fig. 9 (top), indicating the location of the turbulent flame brush, together with iso-contours of OH mass fraction, at 3×10^{-2} and 3×10^{-4}. The average OH* emission image obtained by the EM2C team [7,39] is given at the bottom of Fig. 9, for qualitative comparison (this picture represents emitted OH radicals, which may differ slightly from OH field). The overall shape of the flame is recovered by the simulation, nevertheless, the spreading angle of the flame seems to be slightly under-predicted. In both the LES and the experiment, the flame is not closed at the end of the observation box.

A cut of the average temperature field is given in Fig. 10 (left). Comparison along the dashed lines of Fig. 10 (left) with experimental data from ONERA [8,12] is plotted in Fig. 10 (right). Lines represent LES results and indicate the presence of a hot burning layer surrounding the central oxygen jet. The maximum temperature is around 2400 K. The radial position r of the maximum temperature increases with the distance to the injector x, pointing out that the flame widens and is still open. This is consistent with the experimental observation shown in Fig. 9. Initially, close to the injector, for $x = 15$ mm, the flame is very thin and confined around the oxygen jet. The high-temperature zone broadens as distance from injector is increased.

Symbols in Fig. 10 are experimental results of Habiballah et al. [8,12]. For $x = 15$ and $x = 50$ mm, LES results clearly exhibit strong discrepancies with the experiment, where no flame can be clearly evidenced, since the maximum

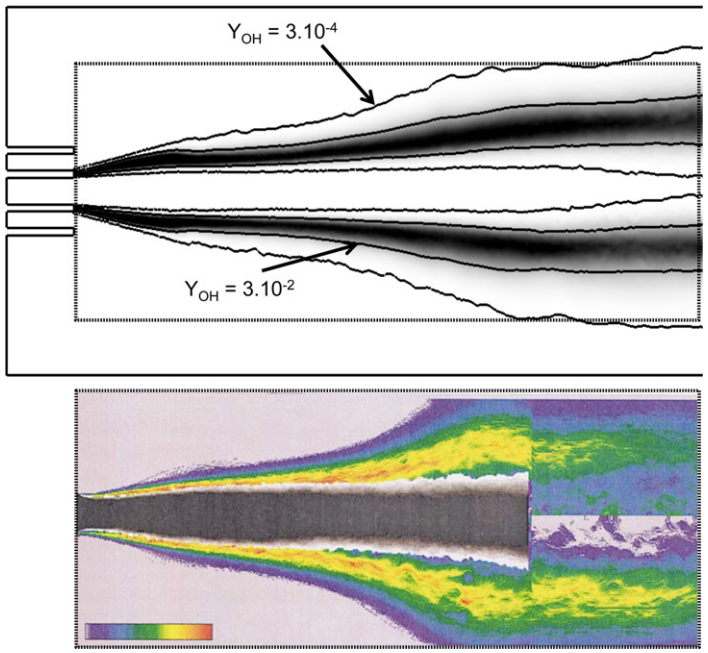

Fig. 9. Section of the average OH mass fraction field in the median plan (top). The length of view is 100 mm. Bottom picture is an averaged OH* emission image obtained by Juniper et al. [39,7].

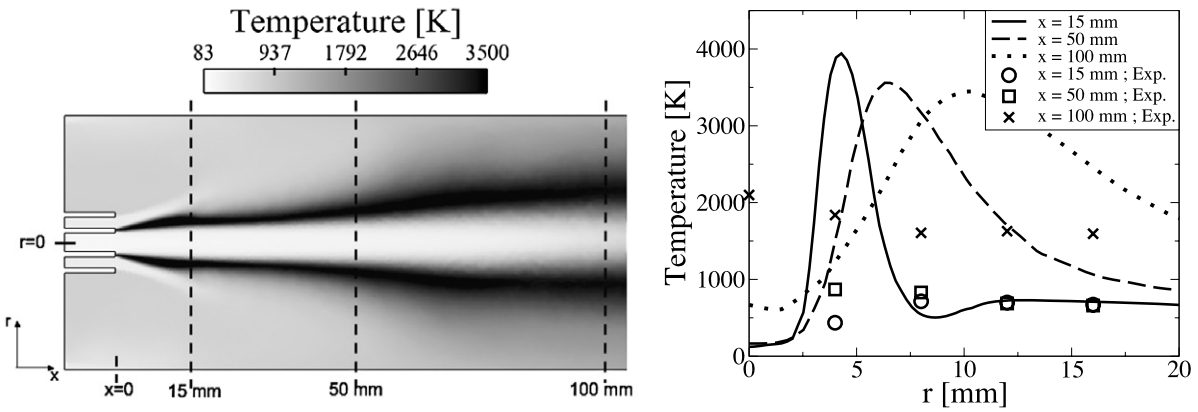

Fig. 10. Left: section of the average temperature field in the median plan. Right: plots of temperature profiles in the radial direction. r is the radial distance from injector centerline and x is the longitudinal distance from injector exit. Symbols are temperatures measured by Habiballah et al. [8,12]. Lines are the LES results.

mean temperature is below 1000 K. As indicated by Habiballah et al. [8], the mean flame temperature is low because the flame is very thin, and is strongly fluctuating. This behavior may not be correctly captured in the LES simulation, because of the required grid resolution. Nevertheless, the previous comparison with mean OH* emission images [7] shows overall good agreements. The CARS measurement technique used in this work [8] probes H2 molecules in the reacting flow and analyses their spectrum of emission from which the temperature of the flow is obtained. Therefore, the validity of the temperature measurement can be questioned in regions of the flow featuring low concentrations of H2 molecules, mainly the LOx dense core for low mixture ratio operating points. At $x = 100$ mm, both LES and experiment indicate temperatures higher than 2000 K, but the maximum value is found at $r = 0$ for experiment, whereas it is located around $r = 10$ mm in the LES. It seems that, at $x = 100$ mm, the flame is closed in the experiment whereas it is not in the simulation.

5. Conclusions

The AVBP solver has been extended to real gas applications by use of a cubic equation of state and the corresponding real-gas thermodynamics. The computation of two single nitrogen jets [4] at supercritical pressure is performed. Two cases from [4] are computed: Case 3, with an injection temperature lower than the pseudo-boiling temperature, and Case 4, with a temperature higher than the pseudo-boiling temperature. As a consequence, the injection density in case 3 is much higher than in case 4 and the dynamics of the jets are highly different, with a potential core equal to 7.9 for case 3 and to 5.1 in case 4. The spreading angle falls close to experiments in case 3, while discrepancies are noticed for case 4. The simulation of a supercritical coaxial LOx/H2 reacting case, from the Mascotte test rig [15], is also performed. Results indicate an initially low-spreading jet over 60 mm, which then widens quickly. The heat release in the shear layer is enhanced by the strong shear and vortical activity between the outer fast hydrogen jet and the central low-velocity oxygen jet. LES results and experimental results of OH^* emission [7] are in good agreement. Comparison with experimental temperature [8] in the first 50 mm shows strong discrepancies, with computed temperature much higher in the simulation than in the experiment. Moreover, experimental temperature measurements seems to indicate that the flame is closed after 100 mm, which is not in accordance with both LES and OH^* emission measurements.

Acknowledgements

The funding for this research is provided by Snecma, which is the prime contractor for European launcher Ariane 5 cryogenic propulsion systems, and CNES (Centre national d'étude spatiale). The authors thank S. Candel (EM2C) and L. Pons (EM2C) and M. Oschwald (DLR) for helpful discussions.

References

[1] J. Hirschfelder, C. Curtiss, B. Bird, Molecular Theory of Gases and Liquids, John Wiley & Sons, 1954.
[2] B.E. Poling, J.M. Prausnitz, J.P. O'Connel, The Properties of Gases and Liquids, fifth edition, McGraw–Hill, 2001.
[3] B. Chehroudi, D. Talley, E. Coy, Visual characteristics and initial growth rate of round cryogenic jets at subcritical and supercritical pressures, Physics of Fluids 14 (2) (February 2002) 850–861.
[4] W. Mayer, J. Tellar, R. Branam, G. Schneider, J. Hussong, Raman measurement of cryogenic injection at supercritical pressure, Heat and Mass Transfer 39 (2003) 709–719.
[5] M. Oschwald, Supercritical nitrogen free jet investigated by spontaneous Raman scattering, Experiments in Fluids 27 (1999) 497–506.
[6] D.W. Davis, B. Chehroudi, Measurements in an acoustically-driven coaxial jet under sub-, near-, and supercritical conditions, Journal of Propulsion and Power 23 (2) (2007) 364–374.
[7] S. Candel, M. Juniper, G. Singla, P. Scouflaire, C. Rolon, Structure and dynamics of cryogenic flames at supercritical pressure, Combustion Science and Technology 178 (2006) 161–192.
[8] M. Habiballah, M. Orain, F. Grisch, L. Vingert, P. Gicquel, Experimental studies of high-pressure cryogenic flames on the Mascotte facility, Combustion Science and Technology 178 (2006) 101–128.
[9] J.J. Smith, G. Schneider, D. Suslov, M. Oschwald, O. Haidn, Steady-state high pressure LOx/H2 rocket engine combustion, Aerospace Science and Technology 11 (2007) 39–47.
[10] G. Singla, Etude des flammes cryotechniques oxygène liquide/méthane à haute pression, Ph.D. thesis, Ecole Centrale de Paris, 2005.
[11] G. Singla, P. Scouflaire, C. Rolon, S. Candel, Planar laser-induced fluorescence of OH in high-pressure cryogenic LOx/GH2 jet flames, Combustion and Flame 144 (2006) 151–169.
[12] L. Vingert, A. Nicole, M. Habiballah, The Mascotte single injector 60 bar hot test for code validation – test-case specifications and some more experimental data, in: Proceedings of the 3rd International Workshop Rocket Combustion Modeling, Snecma, March 2006.
[13] J. Bellan, Theory, modeling and analysis of turbulent supercritical mixing, Combustion Science and Technology 178 (2006) 253–281.
[14] L.C. Selle, N.A. Okong'o, J. Bellan, K.G. Harstad, Modeling of subgrid-scale phenomena in supercritical transitional mixing layers: an a priori study, Journal of Fluid Mechanics 593 (2007) 57–91.
[15] L. Vingert, M. Habiballah, P. Vuillermoz, S. Zurbach, Mascotte, a test facility for cryogenic combustion research at high pressure, in: 51st International Astronautical Congress, Rio de Janeiro, Brazil, 2000.
[16] F.-X. Demoulin, A. Mura, S. Zurbach, Single flow modeling of high-pressure turbulent cryogenic injection and combustion, in: Proceedings of the 3rd International Workshop Rocket Combustion Modeling, Snecma, March 2006.
[17] N. Zong, V. Yang, Cryogenic fluid jets and mixing layers in transcritical and supercritical environments, Combustion Science and Technology 178 (2006) 193–227.
[18] N. Zong, H. Meng, S.-Y. Hsieh, V. Yang, A numerical study of cryogenic fluid injection and mixing under supercritical conditions, Physics of Fluids 16 (12) (2004) 4248–4261.
[19] N. Zong, Modeling and simulation of cryogenic fluid injection and mixing dynamics under supercritical conditions, Ph.D. thesis, Department of Mechanical and Nuclear Engineering, Pennsylvania State University, 2005.

[20] N. Zong, V. Yang, A numerical study of high-pressure oxygen/methane mixing and combustion of a shear coaxial injector, AIAA paper, 2005.
[21] S. Matsuyama, J. Shinjo, Y. Mizobuchi, S. Ogawa, A numerical investigation on shear coaxial LOx/GH2 jet flame at supercritical pressure, in: 44th AIAA Aerospace Sciences Meeting and Exhibit, Reno, Nevada, 2006.
[22] J.C. Oefelein, Thermophysical characteristics of shear-coaxial LOx-H2 flames at supercritical pressure, Proceeding of the Combustion Institute 30 (2005) 2929–2937.
[23] V. Moureau, G. Lartigue, Y. Sommerer, C. Angelberger, O. Colin, T. Poinsot, High-order methods for DNS and LES of compressible multicomponent reacting flows on fixed and moving grids, Journal of Computational Physics 202 (2) (2005) 710–736.
[24] O. Colin, M. Rudgyard, Development of high-order Taylor–Galerkin schemes for unsteady calculations, Journal of Computational Physics 162 (2) (2000) 338–371.
[25] A.G. Kravchenko, P. Moin, On the effect of numerical errors in large eddy simulations of turbulent flows, Journal of Computational Physics 131 (1996) 310–322.
[26] A. Jameson, W. Schmidt, E. Turkel, Numerical solution of the Euler equations by finite volume methods using Runge–Kutta time stepping schemes, AIAA paper 81-1259, in: 14th Fluid and Plasma Dynamic Conference, Palo Alto, 1981.
[27] T. Poinsot, S. Lele, Boundary conditions for direct simulations of compressible viscous flows, Journal of Computational Physics 101 (1) (1992) 104–129.
[28] J.-Ph. Légier, T. Poinsot, D. Veynante, Dynamically thickened flame LES model for premixed and non-premixed turbulent combustion, in: Proceedings of the Summer Program, Center for Turbulence Research, NASA Ames/Stanford Univ., 2000, pp. 157–168.
[29] R.C. Rogers, W. Chinitz, Using a global hydrogen–air combustion model in turbulent reacting flow calculations, AIAA Journal 21 (4) (1983) 586–592.
[30] D. Peng, D.B. Robinson, A new two-constant equation of state, Ind. Eng. Chem. Fundam. 15 (1976) 59–64.
[31] J.C. Oefelein, Large eddy simulation of a shear-coaxial LOx-H2 jet at supercritical pressure, in: 38th AIAA Aerospace Sciences Meeting & Exhibit, Indianapolis, IN, 2002.
[32] T.H. Chung, M. Ajlan, L.L. Lee, K.E. Starling, Generalized multiparameter correlation for nonpolar and polar fluid transport properties, Industrial and Engineering Chemistry Research 27 (4) (1988) 671–679.
[33] K. Harstad, J. Bellan, High-pressure binary mass diffusion coefficients for combustion applications, Ind. Eng. Chem. Res. 43 (2004) 645–654.
[34] F. Nicoud, F. Ducros, Subgrid-scale stress modeling based on the square of the velocity gradient, Flow, Turbulence and Combustion 62 (3) (1999) 183–200.
[35] M. Oschwald, J.J. Smith, R. Branam, J. Hussong, A. Shick, B. Chehroudi, D. Talley, Injection of fluids into supercritical environments, Combustion Science and Technology 178 (2006) 49–100.
[36] R.H. Kraichnan, Diffusion by a random velocity field, Physics of Fluids 13 (1970) 22–31.
[37] A. Smirnov, S. Shi, I. Celik, Random flow generation technique for large eddy simulations and particle-dynamics modeling, Trans. ASME Journal of Fluids Engineering 123 (2001) 359–371.
[38] M. Oschwald, M.M. Micci, Spreading angle and centerline variation of density of supercritical nitrogen jets, Atomization and Sprays 11 (2002) 91–106.
[39] M. Juniper, Structure et stabilisation des flammes cryotechniques, Ph.D. thesis, Ecole Centrale de Paris, 2001.